npj | clean water

Article

Published in partnership with King Fahd University of Petroleum & Minerals

https://doi.org/10.1038/s41545-024-00324-7

A high-throughput approach for assessing antiscaling performance during mineral precipitation from seawater and hard water

A. Poulain[1], R. Besselink[1], A. Fernandez-Martinez[1], M. Kellermeier[2] ✉ & A. E. S. Van Driessche[3] ✉

The undesired precipitation of minerals from solution poses challenges in various industrial and domestic applications, including water treatment, desalination, dishwashers and boilers. To mitigate this, threshold inhibitors - small quantities of water-soluble additives—are commonly employed to inhibit the precipitation of inorganic phases. However, concerns about the persistence of traditional additives like phosph(on)ates) in natural environments and stricter regulations warrant the development of more sustainable alternatives. We present a high-throughput approach using a UV-Vis spectrophotometer and automated data analysis to assess the scale inhibiting potential of numerous candidates and their combinations. The robustness and versatility of this method were validated by measuring the kinetics of alkaline-earth metal carbonates precipitating from simulated hard waters and seawaters across an extended range of experimental parameters. This approach allows for straightforward evaluation and quantification of each antiscaling additive's effectiveness and operational range, enabling direct comparison of different additives and blends of additives. Moreover, it facilitates the study of scaling processes in both bulk solutions and at liquid/solid interfaces. By providing a rapid and reliable means of screening potential additives and formulations, our versatile toolbox will expedite the identification of effective scale inhibitors, thereby contributing to the advancement of sustainable practices in various industries reliant on water treatment and mineral precipitation control.

Uncontrolled precipitation of inversely soluble inorganic salts still represents a major challenge for important industrial applications such as water treatment, desalination, energy production, oil recovery, and others [e.g., ref. 1]. This so-called scaling, or inorganic fouling, also causes serious issues in many domestic appliances such as dishwashers and boilers [e.g., ref. 2]. Usually, scaling occurs when an aqueous solution becomes supersaturated with respect to one or more mineral phases, as a consequence of changes in temperature, pressure, and/or flow. Inorganic compounds relevant to scaling are diverse and include carbonates, sulfates, silicates and oxides [e.g., ref. 3]. Mineralization of these insoluble compounds can severely damage equipment and/or result in critical reductions of productivity, necessitating costly downtimes of facilities for cleaning or repair.

A variety of chemical strategies are commonly employed to prevent, or at least mitigate, the formation of scale under process conditions. The most prominent approaches make use of (i) ion exchangers to remove one or more of the ions involved in scaling [e.g., ref. 4], (ii) sequestrants that form complexes with at least one of the ions [e.g., ref. 5], or(iii) small quantities of water-soluble additives to suppress mineral precipitation [e.g., ref. 6]. The latter concept is by far the most effective and efficient approach. It relies on the influence of so-called threshold inhibitors that are primarily designed to maintain strong interactions with cations present on the mineral surface, through which they greatly delay the precipitation reaction even at sub-stoichiometric concentrations. Such specific interactions can also cause significant modifications of the habit of the formed mineral particles, which

[1]Univ. Grenoble Alpes, Univ. Savoie Mont Blanc, CNRS, IRD, IFSTTAR, ISTerre, 38000 Grenoble, France. [2]BASF SE, Material Science, RGA/BM—B007, 67056 Ludwigshafen am Rhein, Germany. [3]Instituto Andaluz de Ciencias de la Tierra (CSIC-University of Granada), 18100 Armilla, Granada, Spain.
✉e-mail: matthias.kellemeier@basf.com; alexander.vd@csic.es

may alter the propensity of these particles to adhere to the surface of different parts of the equipment (e.g., filters, tube walls or heat exchangers) and thus lead to less severe incrustation. While a wide variety of powerful antiscaling agents have been developed over the years, many of these substances are currently being scrutinized with respect to their ecological profile in view of increased environmental awareness and stricter regulations for use in the respective applications. One prominent example in this context are phosphonates, which provide superior antiscaling performance in e.g., dishwashing processes, but also pose critical environmental issues with regard to eutrophication [e.g., ref. 7]. Consequently, there is a persistent need in the scale inhibitor market for new chemistries that meet the criteria of sustainability (e.g., concerning biodegradation), but still achieve acceptable levels of performance at cost-competitive dose [c.f. refs. 8,9].

One of the limitations in the (re)discovery of effective "green" antiscalants is to probe their potential in preventing scale formation under realistic conditions[9]. The most common approach to do so is based on bulk assays of batch processes, for example by tracking solute depletion (e.g., based on conductivity measurements or elemental analysis) or by characterizing changes in crystal size and morphology via ex- or in-situ microscopy (e.g., optical, scanning electron, or scanning probe) as a function of time (e.g., ref. 10). This, however, only allows a limited number of conditions to be tested and, as such, there is a clear need for methods that probe scale formation for various antiscalant chemistries across an extended space of parameters, yielding reproducible data in a short period of time. From the acquired data, it should moreover be straightforward to deduce the performance and the operational window of the tested additive(s). In this respect, a promising approach is the use of turbidity measurements to determine the induction time of scale precipitation in the presence of antiscalants (e.g., refs. 11–14).

In this work, we have addressed this need and present a high-throughput method for rapid screening of mineral precipitation in the presence of threshold additives under controlled physicochemical conditions. The method is based on absorbance measurements using a multi-cell UV-Vis spectrophotometer and comprises automated procedures for a standardized and robust analysis of the obtained data. We demonstrate the versatility of the approach by screening the effectiveness and efficiency of different antiscaling additives in delaying the precipitation of alkaline-earth metal carbonates from simulated hard waters and seawater. Although the main focus of our study was placed on precipitation processes occurring in the bulk of the solution (contained in UV-Vis cuvettes), we also performed first tests to apply the setup for monitoring scaling on surfaces, namely glass coated with poly(ethersulfone), a common material used as a support for reverse osmosis membranes. The antiscaling agents selected for the proof of concept include neat poly(acrylic) acid as well as industrially modified variants thereof, poly(aspartic) acid etidronic acid, amino-tris(methylene-phosphonic acid) and poly(styrenesulfonate). Data acquired for these additives were evaluated using a custom-designed script enabling their quantitative comparison with respect to antiscaling performance for various physiochemical conditions, both as individual scale inhibitors and in binary combinations. The developed script can easily be adapted to meet particular needs of more complex experiments, rendering the entire setup a promising platform to conduct systematic studies needed to further our understanding of the mechanisms underlying scale formation and its prevention.

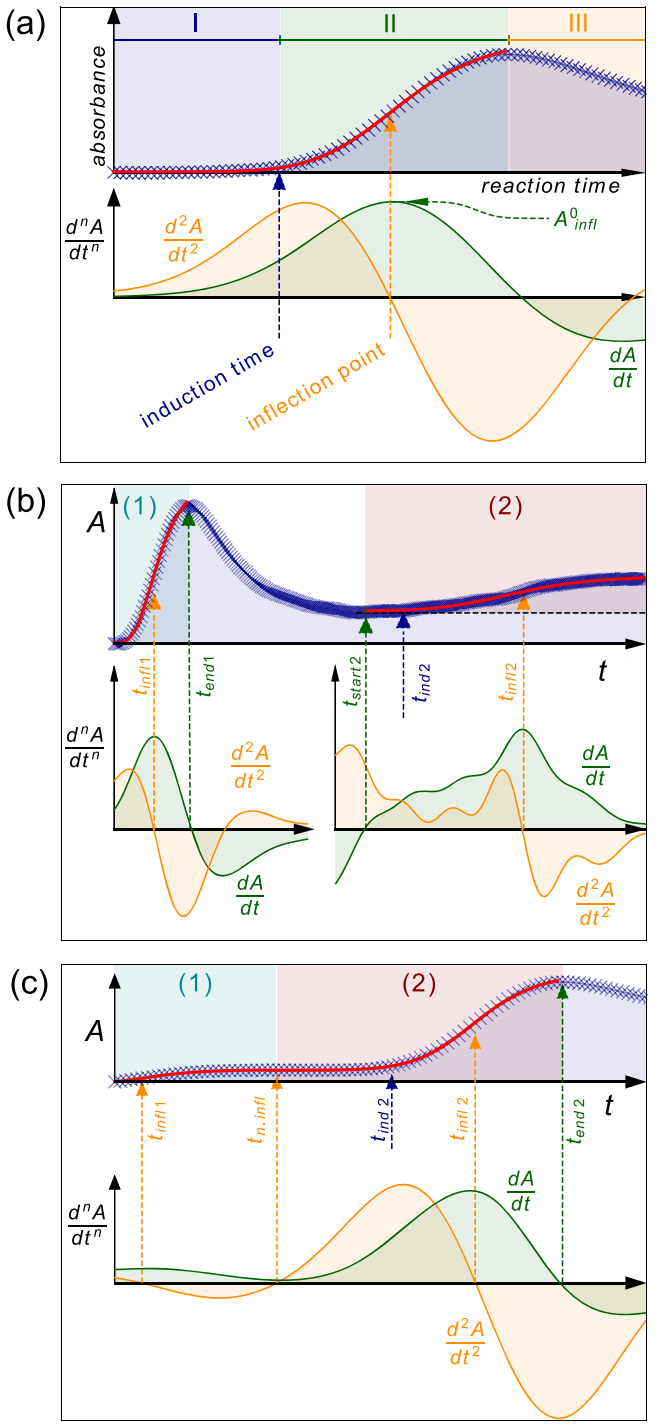

Fig. 1 | Examples of the three types of absorbance profiles observed in this work. These profiles include the first and second derivatives as well as the three characteristic parameters (t_{ind}, A'_{infl} and A_{scale}): (**a**) single-stage nucleation event, (**b**) two nucleation events that are separated from each other by negative values of dA/dt, (**c**) two nucleation events that are solely separated by a negative inflection point.

Results and discussion

Automated data analysis

The first step of the automated data analysis routine was to determine the characteristic parameters t_{ind}, A'_{infl} and A_{scale} from the obtained absorbance curves (cf. Fig. 1a). In some cases, the absorbance curves displayed distinguishable sigmoidal subsections (Fig. 1b, c), which indicate the occurrence of discrete precipitation events (i.e., multistep nucleation). To account for this, our workflow includes a procedure to automatically identify and locate these sigmoidal subsections. Two approaches were used to separate these regions: firstly, subdivisions into sigmoidal time periods were established by searching for negative values in the first derivative, where two regions of higher absorbance are separated by one of lower absorbance (Fig. 1b). To avoid that this procedure becomes too sensitive to noise, both time intervals had to be separated by a minimum number of, e.g., 10, data points with a negative value of dA/dt. Secondly, time periods were also subdivided when a negative inflection point, where dA/dt runs through a minimum and $d^2A/dt^2 = 0$, was found (Fig. 1c). Again, such features were only considered if the concerned region comprised a minimum number of, e.g., 10, data points above a threshold value for A'_{infl} (e.g., >2% of the maximum value of A'_{infl}

over the measured time period). Moreover, to avoid subdivision of the entire transmittance profile into too many subsections, a maximum of three sigmoidal curve sections with the highest values of A_{scale} were accepted, and if possible, merged with neighboring subsections that were rejected.

Subsequently, the absorbance values were normalized by the maximum and minimum values, i.e., $A_{norm} = (A - \min(A)) / (\max(A) - \min(A))$, and net an induction time was assigned to the data point that had at least 4 succeeding data points where both the normalized A_{norm} and dA/dt_{norm} were above a threshold of 5% of their respective maximum value (within the given sigmoidal section). Then, a more accurate value of the induction time was determined by calculating the point where A_{norm} intersects a horizontal baseline through local linear interpolation of the data across a range of four data points from the estimated induction point. For each resulting induction time, the corresponding values for A'_{infl}, i.e., the maximum rate of absorbance increase at the inflection point, and $A_{scale} = A_{max} - A_{min}$, i.e., the degree of total absorbance increase, were determined. Finally, the section with the largest A_{scale} value was considered to be the main precipitation step. We note that this approach also works if the absorbance increases from the beginning of the experiment on, because a minimum starting value for dA/dt was used.

To compare the effectiveness of different antiscaling additives, several precipitation experiments were conducted at various concentrations, which provide characteristic values for t_{ind}, A_{scale} and A'_{infl} as described above. It is assumed that the dependency of the induction time on the additive concentration is (predominantly) controlled by kinetics[15] and can therefore be fitted with the Arrhenius-type model given by Eqs. 1, 4 and 5. This fit provides an integral parameter, $\langle \Delta U_i \rangle$, which reflects changes in the activation energy for nucleation in the presence of an additive. Additives causing a larger increase in activation energy, thus giving higher $\langle \Delta U_i \rangle$ values, can be considered as better antiscalants. The other parameters, A_{scale} and A'_{infl}, which correlate with the amount of mineral scale formed and the rate of nucleation respectively, are expected to decrease with increasing additive concentrations. The characteristic concentration, c^*, at which A_{scale} and A'_{infl} decrease significantly, was determined empirically with an integral breath method[16] (Supplementary Fig. 1).

Figure 2 summarizes the main steps of the data processing routines based on algorithms written in Python 2.0 (a detailed description of the workflow can be found in the Supplementary Information and Supplementary Fig. 2). In essence, two types of files are required as input for the script: (1) raw absorbance curves produced by the UV-Vis spectrometer, and (2) data files containing the physicochemical conditions of the experiments including the used additive concentrations. The script includes various functionalities, which in the first place allow sorting and selecting data, then calculating the derivatives and induction points (also for multi-step nucleation), and finally summarizing the calculated parameters in grouped tables. At this stage, several types of graphical visualizations are available: (i) normalized, smoothed and averaged absorbance plots with standard deviations represented as shaded area, (ii) plots of t_{ind}, A'_{infl} and A_{scale} versus additive concentration, as well as (iii) heat and synergy maps. The flexibility of our Python script enables a profound comparison of the performance of additives at various physicochemical conditions and for different types of salinities (e.g., HW or SW). The script can also handle systems containing two, or more, different types of additives. It can further be adapted to meet particular needs of more complex experimental settings (e.g., to mimic dishwasher solutions containing soil components like proteins or fats etc., or seawater treated in desalination plants that may bring about various organic molecules or bacteria).

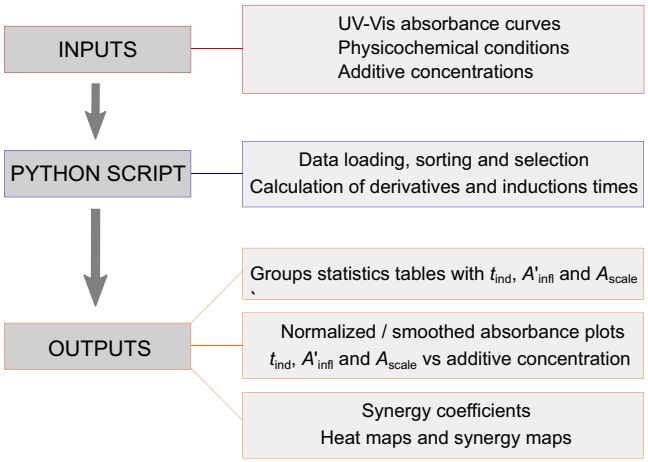

Fig. 2 | Flow chart presenting the main concepts and steps of the Python script developed for advanced data processing.

Influence of type of used UV-Vis cuvettes on the measured induction times

To validate our high-throughput setup and identify technical features that may impact the results, we performed precipitation experiments in five different types of cuvettes (see Methods) and compared the induction times measured for scaling from HW solution in a first test case at T = 23 °C, aragonite saturation indices of 1.71 and various concentrations of polyacrylic acid in a range between 0.00 and 0.03 ppm. For these conditions the main scaling phases were elongated aragonite crystals and cubic calcite crystals. To illustrate differences between the used cuvette types, the measured induction times are divided by the average induction time and represented with a so-called violin plot in Fig. 3. In such a plot, the height of the shape reflects the value distribution, while its width represents the frequency. The largest variation of induction times is observed for optical glass

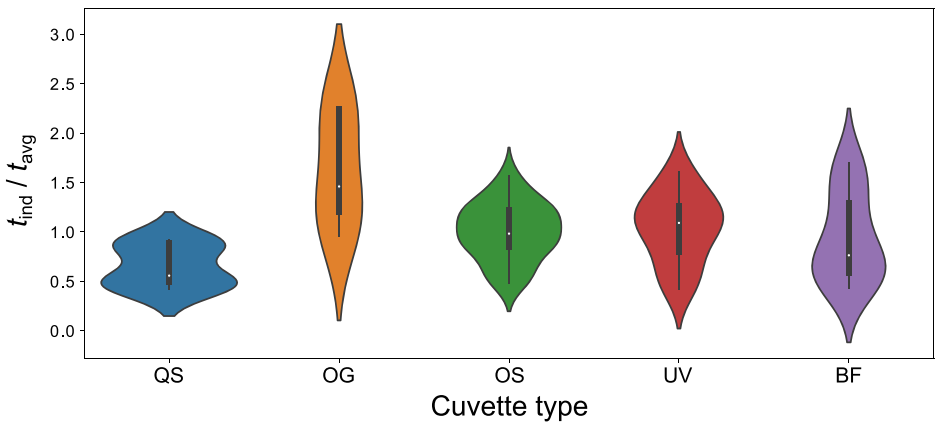

Fig. 3 | Violin plot of induction times measured in different types of UV-Vis cuvettes. The induction are normalized to the respective average value and show the distribution (height) and the frequency (width) of the values. QS quartz glass high performance, OG optical glass, OS special optical glass, UV quartz glass, BF borosilicate glass.

cuvettes (OG), followed by borosilicate cuvettes (BF). The most compact shapes along the vertical direction, reflecting the highest degrees of reproducibility, are observed for high-performance quartz glass (QS) and special optical glass (OS) cuvettes. The superior reproducibility obtained with QS cuvettes could be related to the excellent stirring stability. Consequently, these cuvettes were used for all further measurements conducted with the Lambda 35 spectrometer. Measurements with the AT spectrometer did not require the use of special cuvettes for stirring – even with the OG cells the induction time distribution was much narrower than for experiments with PE (data not shown), most probably due to the more stable stirring behavior achieved with the AT device. These observations highlight the importance of well-defined conditions and proper mixing to obtain reproducible data for a stochastic process such as homogeneous nucleation from solution.

At this point, it should be noted that the hydrodynamic conditions prevailing in 3.5 mL cuvettes as those used here do not necessarily represent the circumstances in real-world applications (e.g., dishwashers or desalination units). This might lead to significant differences in the absolute effects observed for certain additives in each of the distinct settings. However, we are confident that relative trends in the behavior of antiscalants as well as potential synergies between multiple additives should still be valid at the different scale, supporting the use of fast screening tools like the present setup for accelerated development cycles.

Homogeneous mineral precipitation from hard water in the presence of antiscalants

Automated analysis of absorbance profiles. Examples of the smoothed and background-corrected absorbance plots measured for calcium carbonate scaling from hard water (HW) in the absence and presence of Sokalan® CP 50(0–5 ppm) and PSS (0–50 ppm) at pH 8.2 and 60 °C are shown in Fig. 4. Underthese conditions, the HW solution without additive (blue curve) displays a single nucleation step, analogous to the example presented in Fig. 1a, with the following three stages: (i) initial flat part—metastable supersaturated solution; (ii) signal increase—onset of nucleation followed by growth of the nuclei; (iii) plateau of the signal—end of the nucleation and growth phase. In the presence of the modified poly(acrylic acid), a progressive increase of the induction time from 0.3 to 71 min is observed when the additive concentration is increased from 0 to 5 ppm (Fig. 5a). Importantly, Sokalan® CP 50 also changes the mechanisms of precipitation, as evidenced by two steps of turbidity increase already at 1 ppm polymer. Although the particular interactions leading to this behavior are beyond the scope of this work, it is conceivable that the modified poly(acrylic acid) stabilizes nanoscale $CaCO_3$ precursors and prevents their transformation into larger crystalline $CaCO_3$ particles. At a polymer concentration of 5 ppm, the observed singular increase in absorbance is still significantly above the level of noise, but A_{scale} is 3.4 times lower compared to the signal measured in the control experiment without antiscalant. It seems reasonable to assume that the polymer inhibits the precipitation reaction so strongly that only the first precipitation step can be observed during the measurement time of 10 h. For the same experimental conditions, a quite distinct behavior is observed for PSS (Fig. 5b). The induction time is not delayed, even at high additive concentration (50 ppm), while for the same time interval significantly more material seems to precipitate than in an additive-free run (indicated by A_{scale} values). Moreover, there are two domains of different precipitation kinetics (reflected by dA/dt) during scaling at 50 ppm PSS, with faster rates during the onset of precipitation (0 to1 min) and slower growth at later stages (1 to 10 min).

Similar experiments were conducted for all other additives at different HW concentrations, pH values and temperatures in a total of more than 700 experiments (see Methods). Based on visual assessment of turbidity plots such as those shown in Fig. 5, an initial pre-selection can be made to eliminate additives that do not significantly delay or influence the precipitation process. For promising candidates, our automated data analysis routine allows a further rapid evaluation of effectiveness at different physicochemical solution conditions. More specifically, an operational window can be delimited for any given antiscalant through the comparison of t_{ind}, A'_{infl} and A_{scale} values. For well-performing additives, the maximum value of A_{scale} will decrease with increasing additive concentration, and above a critical concentration of antiscalant, the amount (if any) of precipitated material will be insufficient to cause an absorbance increase distinguishable from the noise level. This critical concentration is additive-specific, but it will also depend on the sensitivity of the used spectrophotometer: for example, due to higher noise level in the data collected and/or worse reproducibility caused by imperfect stirring, the experiments will be limited to lower additive concentration ranges. However, such effects do not change the overall trends observed for the selected additives on the two different spectrophotometers, and thus the determination of operational windows is considered to be independent of the used equipment.

An example of the output of our automated data analysis routine is summarized in Fig. 4. It becomes immediately apparent that etidronic acid (EA) outperforms all other antiscalants in HW at pH 8.2 and 60 °C. For dosages ranging from 1 to 5 ppm, the phosphonate always caused the longest induction time (Fig. 4a) and reduced the slope at the inflection point to low values already at 1 ppm (Fig. 4b). The polycarboxylates Sokalan® PA 25 Cl, Sokalan® CP 50 and PAsp also showed considerable retardation of nucleation and decelerated growth with similar degrees of efficiency. PSS, on the other hand, did not change the induction time and instead increased the precipitation rate. Comparing the five additives based on the A_{scale} parameters paints a different picture at first glance, where the polycarboxylates seem to reduce the amount of formed mineral scale more efficiently than EA. However, it has to be considered that A_{scale} depends on the total time of the experiment and therefore, it can only be used for comparison of antiscalant effectiveness if the precipitation reaction has (nearly) been completed (i.e., a plateau in the absorbance curve is reached) during the

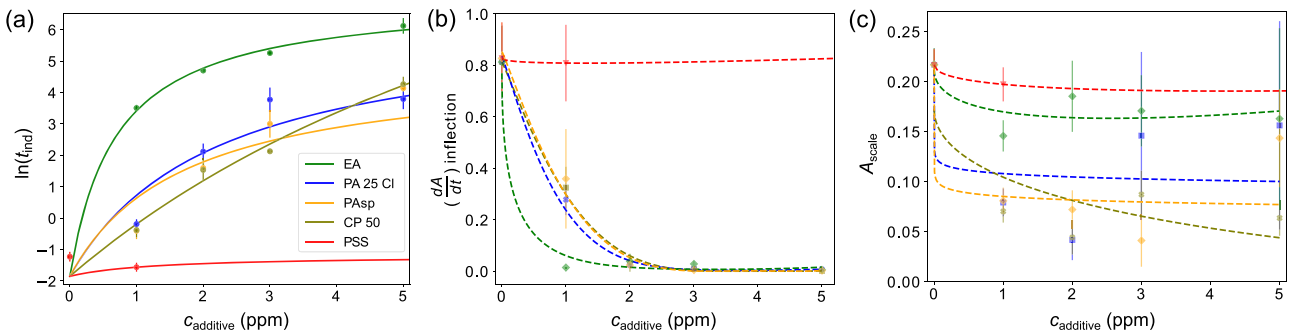

Fig. 4 | Output of automated analyses of absorbance data collected during mineral scale formation in the presence of different additives. Data were obtained from HW at pH 8.2 and 60 °C in the presence of: etidronic acid (EA), Sokalan® PA 25 Cl, PAsp, Sokalan® CP 50 and PSS. **a** Induction time, (**b**) slope at the inflection point, and (**c**) apparent amount of formed scale as a function of additive concentration (0–5 ppm). The dotted lines in (**b**) and (**c**) are based on polynomial fittings and are mere guides for the eye, i.e., they do not have an implicit physical meaning. Error bars indicate the standard deviations.

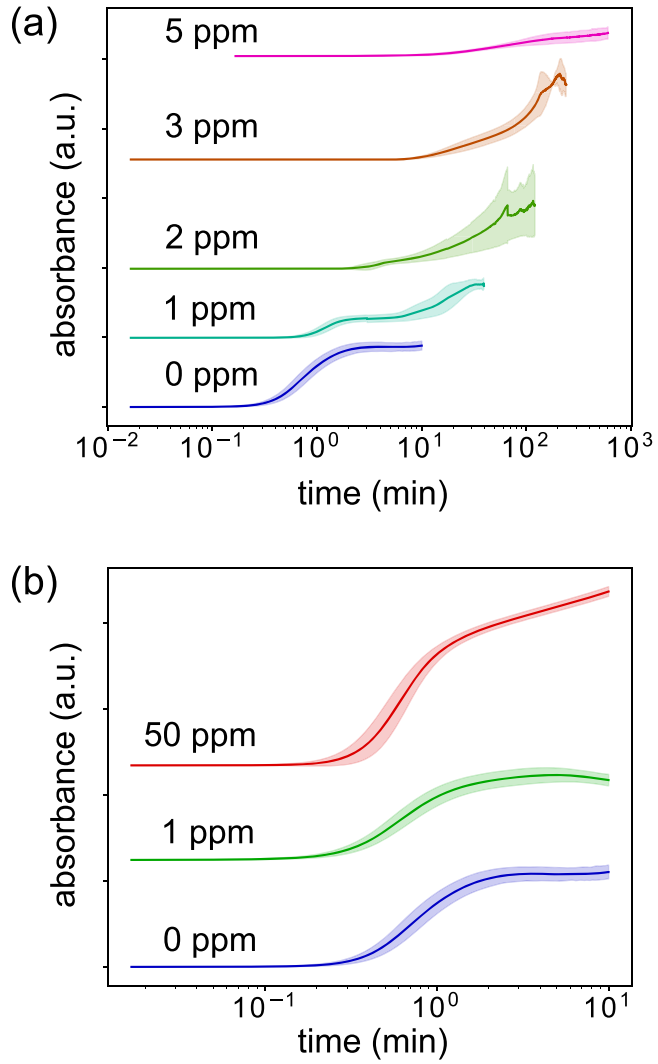

Fig. 5 | Time-dependent absorbance profiles obtained during the formation of mineral scale from hard water in the presence of additives at different concentrations. a Sokalan® CP 50, 0–5 ppm, pH 8.2, 60 °C; (**b**) PSS, 0–50 ppm, pH 10.2, 60 °C. Shaded areas indicate the standard deviations, while the solid line represents the corresponding mean values. An offset of the curves along they-axis was introduced for the sake of clarity.

investigated period of time. Indeed, experiments in the presence of EA were always monitored over much longer intervals than those with the other additives. Hence, the inhibiting potential of EA in terms of A_{scale} is underestimated when compared to the polycarboxylates.

The data shown in Fig. 4 is limited to only one set of physicochemical solution conditions. Although the flexibility of our Python routine allows simultaneous representations of various conditions, too many curves in a single 2D plot complicate the rapid identification of the operational windows for the different additives. To improve the visualization of multiple conditions for various additives, the option of calculating a heat map (or shading matrix) is also available in the data analysis scheme. Heat maps are a visual aid to assess how strongly additives alter the induction time (t_{ind}), the slope at the inflection point (A'_{infl}) and/or the amount of material precipitated (A_{scale}) at a selected antiscalant concentration as a function of the prevailing physicochemical conditions. The heat maps were constructed by normalizing the values for each parameter (t_{ind}, A'_{infl}, A_{scale}) separately and represent them with a color code, where red corresponds to an additive badly performing (i.e., low value) for a given parameter, while green indicates the opposite. An example is presented in Fig. 6 for data obtained from HW at three different pH values (8.2, 9.2 and 10.2) and two temperatures (40 and 60 °C). An additional example of a heat map including all five additives for one set of physicochemical conditions (pH 8.2 at 60 °C) is shown in Supplementary Fig. 3.

For the heat map shown in Fig. 6, a limit of 1 ppm was selected to compare the effectiveness of Sokalan® PA 25 Cl, EA and Sokalan® CP 50 under different solution conditions. However, even at this low additive concentration, precipitation of mineral scale was completely prevented in many cases, especially for EA. Therefore, numerical values were added in the colored rectangles to indicate the highest additive concentration (if <1 ppm) for which nucleation was still detectable with the used setup. In the red-yellow-green color bar scale, dark green rectangles represent effective antiscalants (long t_{ind}, low A'_{infl} and/or low A_{scale}), while poorly performing additives (short t_{ind}, high A'_{infl} and/or high A_{scale}) are highlighted in dark red. This visual "traffic light" approach helps to directly translate experimental data into optimal working conditions. For example, green color prevails in the case of EA, regardless of pH and temperature and usually below the appointed 1 ppm, differentiating its performance from the two poly(acrylic acid)-based products. This suggests that for the tested solution conditions, the phosphonate has the best antiscaling features when applied as single additive, even at low dosage. It should be noted, however, that the inhibition of bulk scaling is not the only function of such additives in real-world applications, where other effects like scale or soil dispersion may play an equally important role. The heat map in Fig. 6 also highlights that all three additives perform significantly better at lower temperature (40 °C)—although the supersaturation of the solutions with respect to $CaCO_3$ phases was adjusted to the same or similar level at both investigated temperatures (see Methods). This emphasizes that soluble additives can change their antiscaling behavior in a subtle manner depending on the chosen conditions. Such differences are readily revealed by the automated data analysis routine developed in this work.

Synergistic effects. Many modern formulations do not contain single antiscaling agents, but rather comprise multiple active components to address different needs in an application and optimize the overall performance. In such "additive cocktails" synergistic effects may occur, i.e., the effectiveness to inhibit mineral precipitation is dramatically increased beyond the simple sum of individual contributions [e.g., ref. 9 In many cases, synergies are found empirically or may be overlooked despite their existence within a certain window of compositions. Thus, modern formulation development requires fast screening and automated analysis tools like the methodology established in the present work to unveil potential synergistic relationships within a chosen set of additives. Heat maps as shown above can help to reveal if the combination of additives brings better (i.e., synergy) or worse performance at any given concentration. However, this type of representation can quickly become too complex and difficult to interpret, especially when comparing different concentration ratios of additives. To overcome this issue, a more intuitive graphical representation of the net effectiveness of "antiscaling cocktails" can be obtained by plotting a 3D map of induction time values measured for different additive ratios and concentrations. An example of synergy trends observed for a combination of Sokalan® PA 25 Cl and EA (in HW at pH 8.2 and 60 °C) and modeled using Eq. 7 are shown in Fig. 7a. In this plot, the x and y axes range from 0 to 5 ppm and represent the concentrations of used EA and PA 25 Cl, while the z axis gives average values of the experimentally determined induction times for both individual additives and their combinations.

To evaluate the degree of potential synergy between the two additives in binary mixtures, Eq. 7 was used to fit the experimentally determined induction time data. The result of the fitting procedure is reproduced in the form of a three-dimensional triangular surface plot (gray-shaded plane) shown in Fig. 8a. In this plot, flat areas linking points of the same concentration indicate compositional space where no synergistic effect occurs, whereas local convex shape would hint at positive interactions between the two additives and a net performance beyond the sum of individual contributions. In turn, concave surfaces would be associated with a negative

Fig. 6 | Performance heat map calculated for different additives. The heatmap includes data of three different additives (Sokalan® PA 25 Cl, etidronic acid and Sokalan® CP 50) at a maximum concentration of 1 ppm. For conditions where precipitation was completely suppressed at 1 ppm, the highest possible concentration of the additive is given in the respective box.

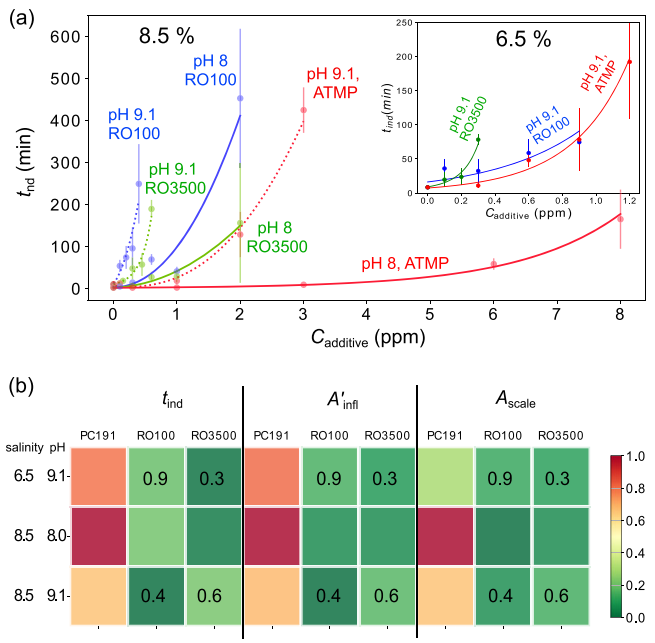

Fig. 7 | Screening of three selected antiscalants during mineral scale formation from synthetic seawater at 40 °C and variable salinity and pH. a Comparison of the induction times measured as a function of additive concentration at salinities of 8.5% (main plot: pH 8.0 (full lines) and 9.1 (dotted lines)) and 6.5% (inset: pH 9.1 only). Error bars indicate the standard deviations. **b** Performance heat map calculated for the three different additives (ATMP, Sokalan® RO 100 and Sokalan® RO 3500) at a maximum concentration of 1 ppm. For conditions where precipitation was completely suppressed at 1 ppm, the highest possible concentration of the additive is given in the respective box.

interference between the additives, where one antiscalant disrupts the performance of the other. In the given example of binary mixtures of EA and Sokalan® PA 25 Cl, neither positive nor negative synergy is observed, as flat lines (within the margin of error) can be drawn between the points of the selected concentrations and the slopes increase monotonously towards the pure EA end member. This demonstrates that under the tested conditions, the induction time is simply the sum of the two effects observed in experiments with the single additives. Although this is (usually) not a desired result, the chosen example nonetheless highlights the potential of the presented approach to identify synergistic interactions in complex antiscaling formulations.

The Arrhenius-type model underlying the analysis discussed above also yields $<\Delta U_i>$as an integral parameter reflecting the antiscaling potential of a given additive across the entire range of conditions studied (cf. Equations 4 and 5). $<\Delta U_i>$values determined for different additives in the HW system are compiled in Table 1. The low antiscaling potential found for PSS (0.1) is consistent with the lack of changes in the induction time discussed for this polymer above. The polycarboxylates Sokalan® PA 25 Cl, Sokalan® CP 50 and PAsp all show similar $<\Delta U_i>$values (1.3–1.5) in line with their comparable performance in the present HW tests. Finally, etidronic acid outcompetes the other antiscalants ($<\Delta U_i> = 2.5$) under the chosen conditions, confirming the insights extracted from the heat maps shown in Fig. 6 and Supplementary Fig. 3. Along similar lines, the value of the cross-term$<\Delta U_{ij}>$can be leveraged as a measure for the additional antiscaling potential (i.e., synergy) brought about by the combination of two additives. The parameter calculated for the 1:1 mixture of EA and Sokalan® PA 25 Cl is within the error equal to zero (−0.03), which confirms the lack of any synergistic effect for this particular antiscalant combination. The remaining fitting parameters derived from the Arrhenius-type model are listed in Supplementary Table 1.

The contribution of each antiscalant component to the synergy integral coefficient of the mixture can be further explored by plotting the individual effects and their cumulative sum, as shown in Fig. 8b. Again, the experimentally determined combined influence of the two additives (green symbols and line in Fig. 8b) is well described by the individual inputs from the polymer (purple) and the phosphonate (red), whereby the latter component shows much stronger impact on the net antiscaling performance. Importantly, the 1:1 mixture of EA and Sokalan® PA 25 Cl achieves nearly the same inhibiting efficiency as pure EA. However, it offers the additional advantage of reducing the phosphonate content by half. This reduction is desirable from an environmental perspective.

Homogeneous and heterogeneous mineral precipitation from seawater in the presence of antiscalants

To further demonstrate the versatility of the newly developed high-throughput methodology, we applied the setup and analysis routines to study the influence of different antiscaling agents on the precipitation of solid mineral phases from synthetic seawater (SW)—a critical process on the surface of reverse osmosis membranes. For this purpose, induction times were determined for two different types of modified poly(acrylic acid)

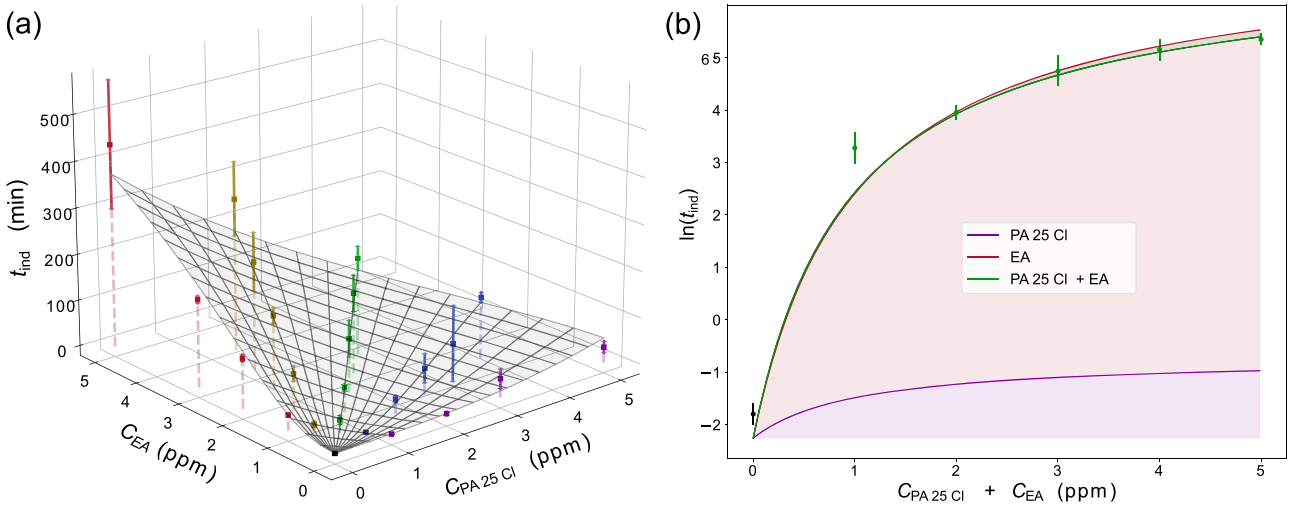

Fig. 8 | Induction times measured for mineral precipitation from HW at pH 8.2 and 60 °C in the presence of different amounts of EA and Sokalan® PA 25 Cl (PAA). a Three-dimensional plot illustrating the influence of the concentrations of EA and PAA (*x* and *y* axes) on the measured induction time (*z* axis) in experiments with single additives (red: EA, purple: PAA) and binary mixtures (green: 1:1, blue: 1:3, green: 3:1) The gray-shaded plane represents the results of data fitting based on the Arrhenius-type model given by Eq. 7. **b** Individual nucleation-inhibiting contributions and their cumulative sum for a 1:1 mixture of EA and PAA. Dots represent experimental data and curves are obtained from Eq. 7. Error bars indicate the standard deviations.

(Sokalan® RO 100 and Sokalan® RO 3500) as well as the low molecular weight additive amino-tris(methylenephosphonic acid) (ATMP). An overview of the data obtained for homogeneous precipitation from synthetic seawater at two different levels of salinities (6.5 and 8.5%) and pH (8.0 and 9.1) in the presence of the three selected additives is shown in Fig. 7. For all tested conditions the main scaling phase was calcium carbonate.

In terms of induction times (Fig. 7a), the best antiscaling performance is observed for Sokalan® RO 100 at pH 9.1 and a salinity of 8.5%, while ATMP shows the weakest scale inhibition at pH 8.0 and a salinity of 8.5%. In general, at a constant salinity of 8.5% all three additives were found more effective at higher pH (9.1 compared with 8.0), with a clear ordering of antiscaling potential according to Sokalan® RO 100 >Sokalan® RO 3500 > ATMP at both studied pH levels. Again, differences in antiscalant performance at distinct levels of pH are per se not expected, because the solution composition (i.e., the calcium and (bi)carbonate content) was adjusted to establish the same degree of supersaturation with respect to aragonite. In turn, at a constant pH of 9.1 the additives Sokalan® RO 3500 and ATMPgain effectiveness when the salinity (and, with it, the degree of supersaturation) is reduced to 6.5%, whereas Sokalan® RO 100 shows somewhat decreased scale inhibition power (see inset in Fig. 7a). All these effects can again be recognized at a glance from the corresponding heat map shown in Fig. 7b, from which the respective operational window can be deduced for each studied additive.

Under realistic application conditions, the formation of mineral scale does often not occur homogeneously in the bulk of a solution (as implicitly assumed in the experiments discussed above), but rather proceeds preferentially through heterogeneous nucleation on foreign surfaces such as the inner walls of tubings or the surfaces provided by reverse osmosis membranes or heat exchangers. To mimic this situation in our UV-Vis setup, we introduced thin and optically transparent substrates with two different types of surface chemistry (glass before and after coating with PES) and measured the induction times of surface-mediated precipitation at 40 °C under static conditions (i.e., no stirring) from SW at a salinity of 8.5% and a pH of 9.1. In a first step, turbidity changes were monitored over time for blank glass and PES-coated glass in contact with pure SW solution in the absence of any antiscalant, while in a second step 0.1 ppm Sokalan® RO 100 was added to the seawater for scaling on PES-coated glass. Although absorbance curves with similar shapes are observed on both substrates without added polymer, a significant increase of the turbidity occurs almost immediately on the PES-coated glass, indicating a shorter induction time compared to untreated glass (Fig. 9). This notion is confirmed by complementary light microscopy images (Supplementary Fig. 4), which show a more dispersed distribution of relatively large (>5 µm) crystals on blank glass, while the PES-coated surface is covered with a high density of considerably smaller particles (<1 µm). This indicates a higher heterogeneous nucleation rate and may be caused by non-uniformities of the PES coating (i.e., chemical and/or structural defects). Addition of 0.1 ppm Sokalan® RO 100 reduces the nucleation rate and the amount of precipitate deposited on PES-coated glass (cf. Fig. 9), but also changes the morphology of the formed crystalline particles, which adopt rounded shapes and seem to be more evenly separated across the substrate (Supplementary Fig. 4). Although more experimental work is required to draw concrete conclusions on antiscalant effects at interfaces, these preliminary results constitute a proof of concept for applicability of our UV-Vis methodology to screen additives for heterogeneous crystallization control.

Table 1 | Integral coefficients $<\Delta U_i>$ characterizing the antiscaling potential of individual additives in the HW system and ΔU_{ij} as a measure for synergistic effects in the 1:1 mixture of etidronic acid (EA) and Sokalan® PA 25 Cl (see text for details)

	coef
$<\Delta U_i>$ *PA 25 Cl*	1.53 ± 0.62
$<\Delta U_i>$ *CP 50*	1.33 ± 0.53
$<\Delta U_i>$ *EA*	2.49 ± 0.52
$<\Delta U_i>$ *PSS*	0.10 ± 0.41
$<\Delta U_i>$*PAsp*	1.42 ± 0.57
$<\Delta U_{ij}>$*EA + PA 25 Cl*	-0.03 ± 0.56

Concluding remarks

Making the proper choice of single or multiple additives for a given set of operational conditions is paramount to optimize the performance of formulations for scale inhibition in different types of processes and applications. If the operational conditions change, most likely the additive(s) and/or its/their dosage(s) will have to be adapted as well, and vice versa. The flexible high-throughput method developed in this work allows formulators to swiftly determine the effectiveness of antiscaling additives over a wide range of experimental conditions (different temperatures, pH values, salinities etc.). The large variety of user-friendly calculation and visualization tools

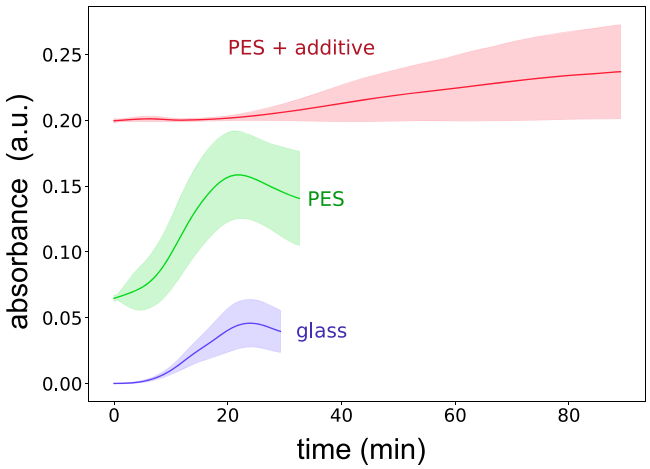

Fig. 9 | Absorbance curves measured during heterogeneous nucleation. Mineral scale forming from synthetic seawater on blank glass (blue), PES-coated glass (green) and PES-coated glass in the presence of 0.1 ppm Sokalan® RO 100 (red). Solid lines represent average values, while the shaded areas indicate the standard deviations.

provided in the form of an open-source Python code further more enables an intuitive and detailed evaluation of the performance patterns of single additives as well as multi-component systems. This approach can be used to probe mineral precipitation in the bulk of a solution or at surfaces. It can also be easily adapted to meet particular needs of more complex experiments or to more closely simulate real-world working conditions, e.g., by including dirt components relevant to dishwasher applications or organics from seawater in desalination processes. As such, the methods presented in this study will contribute to accelerated development cycles in antiscaling research and may also support rationally driven concepts for next-generation antiscalant formulations with sustainable property profiles.

Methods

Preparation of hard water

Synthetic hard water (HW) was prepared at a hardness of 21°dH according to the German Hardness scale, with a Mg:Ca ratio of 3:1. Stock solutions were prepared by dissolving the following commercially available salts (Carl Roth, France) in deionized water: $MgCl_2 \cdot 6H_2O$ and $CaCl_2 \cdot 2H_2O$ ("cationic" stock solution) and $NaHCO_3$ ("anionic" stock solution). The concentration of the added salts was adjusted to ensure a constant supersaturation index with respect to aragonite ($SI_{aragonite} = 1.71$, calculated using the PHREEQC code[17]) for different pH values (8.2, 9.2 and 10.2) and temperatures (40 and 60 °C) (see Table 2). The selected experimental conditions were chosen to represent typical working conditions of domestic appliances such as dishwashers or laundry machines. Before starting the experiments, a specific amount of NaOH was added to the anionic stock solution to adjust the pH of the final hard water to the desired target value.

Preparation of synthetic seawater

Synthetic seawater (SW) was prepared by dissolving the following commercially available salts (Carl Roth, France) in deionized water: NaCl, Na_2SO_4, KCl, $NaHCO_3$, Na_2CO_3, KBr, H_3BO_3, NaF ("anionic" stock solution) and NaCl, KCl, $MgCl_2 \cdot 6H_2O$, $CaCl_2 \cdot 2H_2O$, $SrCl_2 \cdot 6H_2O$ (cationic stock solution), according to the recipe of Kester et al. [18] Two different levels of salinity (6.5% with $SI_{aragonite} = 1.73$ and 8.5% with $SI_{aragonite} = 1.92$) and pH values (8.0 and 9.1) were selected for homogeneous precipitation tests (see Table 3). These tests were performed at 40 °C to accelerate the precipitation kinetics. While the pH of a typical seawater ranges between 7.5 and 8.4 and the total salinity usually amounts to about 3.5%[19], we selected a higher pH value that is representative of those used in desalination plants to improve the effectiveness of the boron removal process during single pass reverse osmosis[20,21] and higher salinities typical of brines formed in reverse osmosis systems. We should note that we have only selected a few conditions that can be encountered during seawater desalination to test our setup. However, if we were to investigate for example scaling in the second step of a two-pass reverse osmosis system, lower salinities should be considered.

Table 2 | Concentrations of $MgCl_2 \cdot 6H_2O$, $CaCl_2 \cdot 2H_2O$ and $NaHCO_3$ in hard water stock solutions (C: cationic solution, A: anionic solution) and supersaturation indices (SI) calculated for distinct calcium carbonate phases at the different chosen pH values and temperatures

Solutions		Concentration in stock solutions [g/L]					
$MgCl_2 \cdot 6H_2O$	C	0.76	0.25	0.13	0.55	0.20	0.12
$CaCl_2 \cdot 2H_2O$	C	1.65	0.53	0.29	1.20	0.43	0.27
$NaHCO_3$	A	1.70	0.55	0.29	1.23	0.44	0.28
pH		8.2	9.2	10.2	8.2	9.2	10.2
temperature (°C)		40	40	40	60	60	60
$SI_{aragonite}$		1.71	1.71	1.71	1.71	1.71	1.71
$SI_{calcite}$		1.84	1.84	1.84	1.83	1.83	1.83
SI_{ACC}		−0.51	−0.51	−0.51	−0.71	−0.71	−0.71

ACC amorphous calcium carbonate.

Table 3 | Composition of the synthetic seawater stock solutions (C: cationic solution, A: anionic solution) and supersaturation indices (SI) calculated for aragonite at the different chosen pH values and salinities

Solutions		Concentration in stock solutions [g/L]		
NaCl		44.43	58.11	58.11
Na_2SO_4		14.89	19.47	19.47
KCl		1.26	1.64	1.64
$NaHCO_3$	C	0.48	1.36	0.63
Na_2CO_3		0.24	0.68	0.32
KBr		0.36	0.48	0.48
H_3BO_3		0.10	0.13	0.13
NaF		0.01	0.02	0.02
NaCl		44.43	58.11	58.11
KCl		1.26	1.64	1.64
$MgCl_2 \cdot 6H_2O$	A	40.23	52.61	52.61
$CaCl_2 \cdot 2H_2O$		5.64	15.80	7.38
$SrCl_2 \cdot 6H_2O$		0.09	0.12	0.12
temperature (°C)		40	40	40
salinity (%)		6.5	8.5	8.5
pH		9.1	8.0	9.1
$SI_{aragonite}$		1.73	1.92	1.92

Antiscaling agents

The following polymeric antiscalants were provided in technical quality by BASF SE: Sokalan® PA 25 Cl (neat poly(acrylic acid), used in dishwashing formulations), Sokalan® CP 50 (modified poly(acrylic acid), used in dishwashing formulations), Sokalan® RO 100 (modified poly(acrylic acid), used in reverse osmosis processes), and Sokalan® RO 3500 (modified poly(acrylic acid), used in reverse osmosis processes). For comparison, neat poly(-aspartic acid) and poly(styrene sulfonate) (PSS) were purchased from Alamanda Polymers and Sigma-Aldrich, respectively. As prominent low molecular weight antiscalants, 1-hydroxyethane-1,1-diphosphonic acid (also referred to as etidronic acid (EA), used in dishwashing formulations)

Table 4 | Characteristics of the selected antiscaling agents and experimental conditions chosen to study their influence on scaling from hard water (HW) and synthetic seawater (SW)

Acronym	Chemistry	MW [g/mol]	pK_a	Type	Measurement conditions		N° exp.
					pH	T / °C	
PA 25 Cl	Poly(acrylic acid)	4000	4.5[a]	HW	8.2, 9.2, 10.2	40, 60	177
CP 50	Modified poly(acrylic acid)			HW	8.2, 9.2, 10.2	40, 60	188
EA	Etidronic acid	206	1.7, 2.47 7.28, 11.41[b]	HW	8.2, 9.2, 10.2	40, 60	132
PSS	Poly(sodium 4-styrenesulfonate)	70000	1[c]	HW	8.2, 10.2	60	105
PAsp	Poly(aspartic acid) (BASF)	5000	3.73[d]	HW	8.2, 10.2	60	78
PAsp	Poly(aspartic acid) (Alamanda)	6800	3.73[d]	HW	8.2, 10.2	60	32
PA 25 Cl+ EA				HW	8.2	60	112
CP 50 + EA				HW	8.2	60	61
PAsp + EA				HW	8.2	60	62
					pH	Salinity / %	T / °C	
RO 100	Modified poly(acrylic acid)			SW	9.1	6.5	40	24
RO 3500	Modified poly(acrylic acid)			SW	8.0, 9.1	8.5	40	52
				SW	9.1	6.5	40	16
					8.0, 9.1	8.5	40	68
ATMP	Amino-tris(methylene phosphonic acid)	299	0.5–1.5[e]	SW	9.1	6.5	40	20
			5.0–6.0		8.0, 9.1	8.5	40	76

[a][20], [b][21], [c][24], [d][25], [e][26–28].

and amino-tris(methylene phosphonic) acid (ATMP, used used in reverse osmosis processes) were obtained from Sigma-Aldrich and Nalco (PermaTreat® PC-191). The characteristics of all selected additives are summarized in Table 4. Their effectiveness in suppressing the formation of alkaline-earth metal carbonate incrustations has been evaluated as a function of temperature and pH. Also, the existence of possible synergistic effects between the additives in binary combinations has been tested at pH 8.2 and 60 °C using hard water solutions. The particular measurement conditions as well as the number of successfully conducted experiments using our high-throughput method are given in Table 4.

Experimental setup for antiscalant screening

The formation of a new (solid) phase in the bulk of a solution (homogeneous case), or on a surface inside of a cuvette (heterogeneous case), will cause an increase in the absorbance of the solution due to a combination of increased light absorption, scattering and reflectivity. Changes in the absorbance (A) during the precipitation of minerals from HW or SW solutions in the presence and absence of additives were recorded using two multicell UV-Vis spectrophotometers (Perkin Elmer Lambda 35(PE) or Agilent Technologies Cary 3500 (AT)) providing temporal resolutions ranging from 1 s to 0.1 min per data point. A schematic view of the setup is shown in Supplementary Fig. 5. All measurements were carried out at a wavelength of 540 nm using 6 (PE) or 7 (AT) cuvettes simultaneously. Temperature was controlled using a Peltier-thermostatted multicell module PTP-6 (PE) or an integrated air-cooled Peltier system (AT).

For bulk precipitation experiments (i.e., the homogeneous case), the cationic stock solution, containing the desired amount of an additive (0 to 50 ppm), was preheated inside the temperature-controlled cuvette holder of the UV-Vis spectrophotometer, while the anionic part (containing the necessary amount of NaOH for pH adjustment) was preheated in an external temperature-controlled water bath. Once the desired temperature was reached for both solutions, the anionic solution was injected into the cuvettes at a 1:1 volume ratio with respect to the cationic solution. The UV-Vis measurement was started immediately after mixing of the two solutions. During all bulk precipitation experiments, the solution in the cuvettes was continuously stirred by means of an immersed magnetic bar. A blank sample was measured simultaneously to correct (if needed) for machine artefacts and signal instability. Data collection was carried out until a stable plateau was reached in the absorbance signal or up to a maximum of 20 h of measurement. Each experiment was repeated at least 6 times to be able to extract meaningful averages.

Surface-induced precipitation (i.e., the heterogeneous case) was studied with untreated and poly(ethersulfone)-coated glass slides placed in cuvettes filled with SW solutions. Polymer-coated glass was prepared by dissolving 0.5 g PES(poly(oxy-1,4-phenylenesulfonyl-1,4-phenylene), Sigma-Aldrich) in 25 mL N-methyl-pyrrolidone (NMP, Sigma-Aldrich, >99%). Standard microscopy glass slides were cut to a width of 7 mm and thoroughly cleaned with concentrated sulfuric acid, water and ethanol. After drying in a flow of compressed air, the clean glass slides were immersed into the PES solution for 30 s. Subsequently, excess coating solution was removed using paper tissue and the coated substrate was dried with compressed air. Finally, the glass substrates were further dried over night at 220 °C to remove all remaining NMP. A 2 mm long flexible silicon rubber hose with an inner and outer diameter of 6 and 10 mm, respectively, was used to immobilize the glass substrate inside of a UV-Vis cuvette perpendicular to the light path. Both the rubber hose and the non-coated glass slide were washed with 1 M hydrochloric acid (prepared from concentrated HCl (Roth, 37%)), deionized water and ethanol (Sigma Aldrich, ≥99.8%), followed by drying in a flow of compressed air. Before each experiment, the anionic and cationic solutions were preheated to 40 °C and premixed in a separate 5 mL vessels. Subsequently, a fixed amount (2 mL) of the mixed solution was transferred into the UV-Vis cuvettes using a 5 mL Eppendorf pipette. All surface-induced precipitation experiments were conducted at 40 °C under static conditions (i.e., no stirring).

UV-Vis cuvettes

The shape of a time-resolved absorbance curve may depend on the stability of the stirring system in the UV-Vis spectrophotometer as well as on the shape and size of the stirrer bar, the cuvette type and the cleaning procedures. Therefore, to ensure meaningful comparison measurements are best performed using comparable conditions.

Table 5 | Different types of cuvettes tested with the PE spectrometer

Material code	Cuvette material	Spectral range [nm]	N° of measurements
QS	High-performance quartz glass[a]	200–2500	9
OG	optical glass	360–2500	5
OS	special optical glass	320–2500	32
UV	quartz glass	260–2500	18
BF	borosilicate glass	330–2500	12

[a]Includes a circular recess at the bottom of the cuvette designed specifically for use with magnetic stirrers.

The following features of an optical cuvette may affect the reproducibility of the UV-Vis data: (i) choice of the cuvette material, (ii) mechanical and chemical resistance against scratch formation (as possible sites for preferential nucleation), (iii) geometry of the bottom part (square or U-shape, potentially influencing the mixing behavior), and/or (iv) the presence of special material at the bottom to improve stirring stability. Five different cuvette types, all with an optical path length of 10 mm and a volume of 3.5 mL, were tested in this study to obtain distributions of induction times in bulk precipitation experiments using the PE spectrometer. While all measurements were carried out at 540 nm, the entire possible spectral ranges for the cuvettes are given in Table 5.

Time-resolved absorbance curves

Precipitation of a new (solid) phase will result in an increase in the light scattered at various angles and, as a consequence, an increased measured absorbance, due to the difference of the refractive indices of the newly formed phase and the surrounding liquid. Therefore, this signal can be utilized to detect the early stage of mineral precipitation from solution.

Time-resolved absorbance curves acquired during a precipitation process can be divided into the following three stages, as illustrated by the example shown in Fig. 1a (I) an induction period in which no new phase has formed yet and the absorbance remains constant at a close-to-zero level; (II) the nucleation stage during which new material nucleates and grows, leading to a detectable increase in absorbance; and (III) a post-nucleation stage where no significant amounts of new particles are formed anymore and the absorbance remains constant or decreases due to segregation or phase transformation. From an individual sigmoidal absorbance profile, a number of parameters can be derived to characterize the precipitation process, including the induction time (t_{ind}), the rate of absorbance increases at the inflection point (A'_{infl}), and the overall absorbance increase (here also referred to as absorbance scaling parameter, A_{scale}), as described in more detail below.

When two stock solutions with a pre-adjusted pH are mixed, the final mixture—here either hard water or synthetic seawater—becomes supersaturated with respect to solid calcium carbonate at the chosen levels of pH and temperature. Depending on the degree of supersaturation and the interfacial energy of the initially nucleated $CaCO_3$ phase, the onset of precipitation is not necessarily instantaneous, giving rise to a so-called induction time (t_{ind} in Fig. 1a). In this work, we define t_{ind} as the time elapsed between the generation of a supersaturated solution and the first observed significant increase in the absorbance signal (Stage I in Fig. 1a). This induction time reflects the transition from a metastable supersaturated solution to a thermodynamically more stable state through phase separation. Subsequently, the new phase continues to nucleate and/or grow (and/or transform), leading to an increase in the measured absorbance (Stage II in Fig. 1a). The maximum rate of absorbance increase corresponds to the slope of the time-dependent absorbance profile at the inflection point (A'_{infl} in Fig. 1a), while the overall increase in the absorbance signal at the end of the precipitation process reflects the amount of formed material (A_{scale} in Fig. 1a). Given the complexity of the scattering process, quantifying the amount of precipitated material is difficult. Nevertheless, these parameters can provide a useful qualitative comparison between similar samples, with for instance different concentrations of antiscaling agents. Ideally, antiscaling agents do not only delay the precipitation process but also reduce the amount of the formed solid phase(s). As such, an effective antiscalant additive will be characterized by a prolonged induction time, a reduced slope at the inflection point and a small quantity of finally precipitated material.

Under realistic conditions, the formation of the final (stable) phase can take place in several steps, as reported for a variety of mineral systems in the literature (e.g., refs. 22,23). Such multistep crystallization mechanisms may or may not involve ample dissolution-reprecipitation processes and thus became manifest in our present time-dependent absorbance measurements in two distinct ways: (i) Significant dissolution (or sedimentation) of the formed particles between two nucleation events, leading to negative values of the first derivative of the absorbance (Fig. 1b); and (ii) no or slow dissolution, resulting in constant (or slightly increasing) absorbance readings and negative values in its second derivative (Fig. 1c).

Model for extracting antiscaling effectiveness from induction times

The effectiveness of antiscaling agents can be rapidly assessed by measuring induction times as a function of supersaturation and other physicochemical solution properties such as, pH, temperature or additive concentration. Recent experimental work suggests that in the specific case of threshold inhibitors, the nucleation process is delayed due to a decrease in the probability of (successful) collisions between atoms/molecules/clusters through e.g., a reduced diffusion rate or increased steric hindrance[15]. This implies that such additives increase the activation energy of the nucleation process. Hence, the relation between supersaturation and induction time is (in part) governed by kinetics (i.e., the attachment rate of ions/molecules/clusters) and can thus be approximated by an Arrhenius-like equation with a linear relationship between the natural logarithm of the induction time and the activation energy. The model implemented in our analysis routine to account for this dependency is of the following general form:

$$\ln\left(t_{ind}\right) = \ln(S) + \Delta\epsilon_i \cdot \theta_i \tag{1}$$

where t_{ind} is the induction time, S a scaling constant related to the activation energy, $\epsilon = E_a/RT$, K the binding constant of the additive to nucleation species, θ the surface coverage of additive i at the surface of a particle and $\Delta\epsilon_i$ a term that describes the change in activation energy due to the adsorption of an additive i ($\Delta\epsilon_i = \Delta E_a/RT$). In some cases and depending on the type of additive θ was not constrained by a limiting saturation equilibrium and therefore proportional to the additive concentration:

$$\theta_i = K \cdot c_i \tag{2}$$

where K is an equilibrium constant and c_i is the concentration of a particular additive. In other cases the additive was found to become less effective for increasing concentrations which could be described by a Langmuir isotherm:

$$\theta_i = \frac{K \cdot c_i}{1 + K \cdot c_i} \tag{3}$$

These equations describe the effect of one or more antiscalants at certain concentrations under the assumption that each additive acts independently. To account for different additive concentrations, we

introduce an integral parameter $<\Delta U_i>$, which can be used as an average response to evaluate the effectiveness of an antiscalant and is defined as follows:

$$\langle \Delta U_i \rangle = \frac{\int_0^{c_i^{max}} \frac{\Delta E_a(c_i)}{RT}\, dc_i}{\int_0^{c_i^{max}} c_i\, dc_i} = \left\{ \begin{array}{l} without\ saturation\ equilibrium: \quad \Delta\mu_i \end{array} \right. \tag{4}$$

$$\langle \Delta U_i \rangle = \frac{\int_0^{c_i^{max}} \frac{\Delta E_a(c_i)}{RT}\, dc_i}{\int_0^{c_i^{max}} c_i\, dc_i} = \left\{ \begin{array}{l} with\ saturation\ equilibrium: \quad \frac{2\cdot\Delta\mu_i\cdot\left(K_i\cdot c_i^{max}-\ln\left(1+K_i\cdot c_i^{max}\right)\right)}{\left(K_i\cdot c_i^{max}\right)^2} \end{array} \right. \tag{5}$$

where $\Delta\mu_i = \Delta\epsilon_i \cdot K_i$. By including a term for the concentration of the antiscalant in the 'weighting' integral, $<\Delta U_i>$becomes independent of the particular (maximum) concentration of additive used in the experiments—even in the absence of a saturation equilibrium for θ.

Equation 1 can be further extended to account for a situation where the influence of multiple additives is not independent and synergistic effects may occur, which are represented by corresponding cross-terms:

$$\ln\left(t_{ind}\right) = \ln(S) + \frac{\sum_{i=1}^{n} \Delta\mu_i \cdot c_i + \sum_{j=1}^{m-1}\sum_{k=j+1}^{m} \Delta\mu_{jk} \cdot \sqrt{c_j \cdot c_k}}{1 + \sum_{i=1}^{n} K_i \cdot c_i + \sum_{j=1}^{m-1}\sum_{k=j+1}^{m} K_{jk} \cdot \sqrt{c_j \cdot c_k}} \tag{6}$$

The square root was placed over the concentration product of the synergy term such that the synergetic constants μ_{jk} and K_{ik} have the same unit as non-synergetic constants μ_j and K_i. To obtain the effect of synergy on the induction time the contribution of the individual additives needs to be subtracted from the equation as illustrated below:

$$\begin{aligned} \ln\left(t_{ind}^{syn}\right) &= \ln\left(t_{ind}^{mix}\right) - \ln\left(t_{ind}^{pure}\right) \\ &= \frac{\sum_{i=1}^{n} \Delta\mu_i \cdot c_i + \sum_{j=1}^{m-1}\sum_{k=j+1}^{m} \Delta\mu_{jk} \cdot \sqrt{c_j \cdot c_k}}{1 + \sum_{i=1}^{n} K_i \cdot c_i + \sum_{j=1}^{m-1}\sum_{k=j+1}^{m} K_{jk} \cdot \sqrt{c_j \cdot c_k}} - \frac{\sum_{i=1}^{n} \Delta\mu_i \cdot c_i}{1 + \sum_{i=1}^{n} K_i \cdot c_i} \end{aligned} \tag{7}$$

Data availability

The data sets generated and analyzed during the current study are available from the corresponding authors on reasonable request.

Code availability

Code available from the corresponding author upon reasonable request.

Received: 30 January 2023; Accepted: 25 March 2024;
Published online: 13 April 2024

References

1. Amjad, Z. & Demadis, K. D. *Mineral scales and deposits: Scientific and Technological Applications* (Elsevier, 2015).
2. Richards, C. S., Wang, F., Becker, W. C. & Edwards, M. A. A 21st-century perspective on calcium carbonate formation in potable water systems. *Environ. Eng. Sci.* **35**, 143–158 (2018).
3. MacAdam, J. & Jarvis, P. Water-formed scales and deposits: types, characteristics, and relevant industries. In *Mineral Scales and Deposits: Scientific and Technological Approaches* 1st ed. (eds Amjad, Z., Demadis, K. D.) pp 3−47 (Elsevier, 2015).
4. German, M. S., Dong, H., Schevets, A., Smith, R. C. & SenGupta, A. K. Field validation of self-regenerating reversible ion exchange-membrane (RIX-M) process to prevent sulfate and silica fouling. *Desalination* **469**, 114093 (2019).
5. Knepper, T. P. Synthetic chelating agents and compounds exhibiting complexing properties in the aquatic environment. *Trac. Trend Anal. Chem.* **22**, 708–724 (2003).
6. Yu, W., Song, D., Chen, W. & Yang, H. Antiscalants in RO membrane scaling control. *Water Res.* **183**, 115985 (2020).
7. Nowack, B. Environmental chemistry of phosphonates. *Water Res.* **37**, 2533–2546 (2003).
8. Hasson, D., Shemer, H. & Sher, A. State of the art of friendly "green"scale inhibitors: a review article. *Ind. Eng. Chem. Res.* **50**, 7601–7607 (2011).
9. Chhim, N. et al. Performance of green antiscalants and their mixtures in controlled calcium carbonate precipitation conditions reproducing industrial cooling circuits. *Water Res.* **186**, 116334 (2020).
10. Sannia, O. S., Bukuaghangin, O., Charpentier, T. V. J. & Neville, A. Evaluation of laboratory techniques for assessing scale inhibition efficiency. *J. Petrol. Sci. Eng.* **182**, 106347 (2019).
11. Shih, W.-Y., Albrecht, K., Glater, J. & Cohen, Y. A dual-probe approach for evaluation of gypsum crystallization in response to antiscalant treatment. *Desalination* **169**, 213–221 (2004).
12. Tantayakom, V., Sreethawong, T., Fogler, H. S., de Moraes, F. F. & Chavadej, S. Scale inhibition study by turbidity measurement. *J. Colloid Interface Sci.* **284**, 57–65 (2005).
13. Shih, W.-Y. et al. Ranking of antiscalant performance for gypsum scale suppression in the presence of residual aluminum. *Desalination* **196**, 280–292 (2006).
14. Zhou, B., Liu, J., Li, L., Chen, X. & Sun, W. 2010 Evaluation Method for Performance of Reverse Osmosis Antiscalants Based on the Turbidity. *International Conference on Electrical and Control Engineering* pp. 926–929 (2010).
15. Nicoleau, L., Van Driessche, A. E. S. & Kellermeier, M. A kinetic analysis of the role of polymers in mineral nucleation. The example of gypsum. *Cem. Concr. Res.* **124**, 105837 (2019).
16. Guinier, A. X-ray diffraction. in *Crystals, imperfect Crystals and amorphous bodies* (Dover Publications Inc., 1994).
17. Parkhurst, D. L. & Appelo, C. A. J. Description of input and examples for PHREEQC version 3--A computer program for speciation, batch-reaction, one-dimensional transport, and inverse geochemical calculations: U.S. Geological Survey Techniques and Methods, book 6, chap. A43, 497. available only at http://pubs.usgs.gov/tm/06/a43 (2013).
18. Kester, D. R., Duedall, I. W., Connors, D. N. & Pytkowicz, R. M. Preparation of artificial seawater. *Limnol. Oceanogr.* **12**, 176–179 (1967).
19. Chester, R. & Jickells, T. D. *Marine Geochemistry* 3rd edn (Wiley-Blackwell, 2012).
20. Güler, E., Kaya, C., Kabay, N. & Arda, M. Boron removal from seawater: state-of-the-art review. *Desalination* **356**, 85–93 (2015).
21. Redondo, J., Busch, M. & De Witte, J.-P. Boron removal from seawater using FILMTECTM high rejection SWRO membranes. *Desalination* **156**, 229–238 (2003).
22. De Yoreo, J. J. et al. Crystallization by particle attachment in synthetic, biogenic, and geologic environments. *Science* **349**, 1–9 (2015).
23. Van Driessche, A. E. S., Kellermeier, M., Benning, L. G. & Gebauer, D. *New Perspectives on Mineral Nucleation and Growth: From Solution Precursors to Solid Materials* 1st ed (Springer, 2017).
24. Michaels, A. S. & Morelos, O. Polyelectrolyte adsorption by Kaolinite. *Ind. Eng. Chem.* **47**, 1801–1809 (1955).
25. European Chemicals Agency. http://echa.europa.eu/ 2024.
26. Mao, L., Ma, C., Gao, J. & Shen, J. Preformed microcapsules for loading and sustained release of ciprofloxacin hydrochloride. *J. Control. Release* **104**, 193–202 (2005).
27. Ostolska, I. & Wiśniewska, M. Comparison of the influence of polyaspartic acid and polylysine functional groups on the mechanism

of polymeric film formation at the Cr2O3—aqueous solution interface. *Appl. Surf. Sci.* **311**, 734–739 (2014).
28. Villemin, D. & Didi, M. A. Aminomethylenephosphonic acids. syntheses and applications (a review). *Orient. J. Chem.* **31**, 01–12 (2015).

Acknowledgements

The authors thank Heike Weber, Roland Ettl and Matthias Arndt (BASF SE) for fruitful discussions on scale inhibition phenomena in automatic dishwashing applications, as well as Stephan Nied (BASF SE) for his valuable guidance in the selection of conditions and additives relevant to scale formation in reverse osmosis processes. A.E.S.V.D. and A.F.M. acknowledge project PROYEXCEL_00771 - SMART-water, with funding from the Consejería de Universidad, Investigación e Innovación, the competent authority in R&D of the Junta de Andalucía.

Author contributions

A.P. data acquisition, analysis, and interpretation, drafting of the manuscript. R.B. model coding, data acquisition and analysis, drafting of the manuscript. A.F.M. acquisition of funding, conception and design of the work, interpretation of data, revising the manuscript. M.K. acquisition of funding, conception and design of the work, interpretation of data, revising the manuscript. A.E.S.V. acquisition of funding, conception and design of the work, interpretation of data, drafting and revising the manuscript.

Competing interests

The authors declare no competing interests.

Additional information

Supplementary information The online version contains supplementary material available at https://doi.org/10.1038/s41545-024-00324-7.

Correspondence and requests for materials should be addressed to M. Kellermeier or A. E. S. Van Driessche.